Particle & Particle Systems Characterization
www.particle-journal.com

Investigation of Interfacial Charge Separation at PbS QDs/(001) TiO_2 Nanosheets Heterojunction Solar Cell

Elham Ghadiri, Bin Liu, Jacques-E. Moser, Michael Grätzel, and Lioz Etgar**

In the recent years, the heterojunction solar cells based on quantum dots (QDs) have attracted attention due to strong light absorbing characteristics and the size effect on the bandgap tuning. This paper reports on the kinetics of interfacial charge separation of PbS QDs/(001) TiO_2 nanosheets heterojunction solar cells. PbS QDs are deposited using a bifunctional linker molecule on two different TiO_2 films, i.e., TiO_2 nanosheets (with 001 dominant exposed facet) and TiO_2 nanoparticles (with 101 dominant exposed facet). Upon bandgap excitation, electrons are transferred from the PbS QDs conduction band to the lower lying conduction band of TiO_2. Based on the ultrafast pump-probe laser spectroscopy technique, the kinetics of charge separation is scrutinized at the PbS/TiO_2 interface. The interfacial charge separation at PbS/TiO_2 nanosheets films made of (001) dominant exposed facets is five times faster than that on (101) dominant exposed facets TiO_2 nanoparticles. The quantum yields for charge injection are higher for the (001) TiO_2 nanosheets than the (101) TiO_2 nanoparticles due to enhanced interfacial interaction with (001) surface compared to the (101) nanoparticles. The superior interfacial charge separation at PbS/(001) nanosheets respect to PbS/(101) nanoparticles is consistent with the higher photocurrent and enhanced power conversion efficiency in the PbS QDs/(001) TiO_2 heterojunction solar cell. The use of (001) TiO_2 nanosheets can be a better alternative to conventional mesoporous TiO_2 films in QD heterojunction solar cells and perovskites-based heterojunction solar cells.

1. Introduction

Quantum dots (QDs) have optical bandgaps that are tunable across a wide range of energy levels by changing the QD size. This is in contrast to bulk semiconductor materials, where the bandgap is fixed by the choice of material composition. Semiconductor QDs of the group IV-VI, such as PbS and PbSe are showing strong absorption in the visible and near-infrared region. PbS QDs have high dielectric constant, small electron, and hole effective mass and large Bohr radius of 18 nm.[1–3] The optical absorption by the bandedge excitonic transition can be tuned between 0.3 and 2 eV with a large absorption cross-section (10^{-15} cm^2) and high luminescence quantum efficiency of about 80%.[4] The tunable bandgap over wide energy range is one great advantage of applying QDs as light- harvesting materials in solar energy conversion systems.[5] Size-dependent optical properties, high optical extinction coefficient, and new concepts of multiple exciton generation[6] in QDs or quantum wells to overcome Shockley-Queisser limit for power conversion efficiency are unique advantages of using QDs over other systems for energy-conversion applications.

Several possible structures have been shown for QDs-based solar cell, sensitized QDs solar cells, QD Schottky solar cells, and QDs heterojunction solar cells. The structure of QD heterojunction solar cell composed of mesoscopic TiO_2 bottom layer, which acts as electron collector layer. The top layer is made of QDs that absorb the light. A metal contact usually gold or silver is deposited on top of the QDs layer to collect the holes. Recent investigations on depleted QDs hetrejunction solar cells include varying the size of the QDs.[7,8] application of TiO_2 or ZnO thin films,[9–11] surface treatments of the QDs.[5] Moreover new morphologies of the TiO_2 in QDs-based solar cells have been investigated such as TiO_2 nanosheets with (001) facets,[12] nanofibers,[13,14] or nanotubes,[5] which show superior behavior as electron acceptor layer in contact with dye or QDs as sensitizers. Recently organo-lead halide perovskite was demonstrated to be an efficient light harvester in the solar cell, in one of the pioneer works, the perovskite was used on TiO_2 with (001) dominant facets.[15] Although the application of dye molecules[16] and QDs[12] with (001) TiO_2 nanosheets improved the cell performance, the kinetics of interfacial charge separation at the QD or the dye with (001) TiO_2 nanosheets has never been investigated.

The heterogeneous charge-separation process is a key process, which results in the current generation through the cell. Kamat and co-workers[17,18] studied the electron injection process from CdSe QDs to TiO_2 nanoparticles. They demonstrated that the vectorial electron-transfer rate is affected by the QDs particle size and the conduction band energy position. Due to the relative smaller electron effective mass than holes effective

Dr. E. Ghadiri, Prof. J.-E. Moser
Photochemical Dynamics Group
Ecole Polytechnique Fédérale de Lausanne
CH-1015, Lausanne, Switzerland
Prof. B. Liu
Department of Chemical
and Biomolecular Engineering
National University of Singapore
Singapore
Prof. M. Grätzel, Prof. L. Etgar
Laboratory for Photonics and Interfaces
Institute of Chemical Sciences and Engineering
Ecole Polytechnique Fédérale de Lausanne
CH-1015, Lausanne, Switzerland
E-mail: michael.graetzel@epfl.ch; lioz.etgar@mail.huji.ac.il

DOI: 10.1002/ppsc.201400210

mass, quantization has more impact on the energy level of electrons rather than holes in these QDs. Therefore, CdSe QDs with smaller size are expected to have favorable conduction band energies for injecting electrons into TiO_2. Hyun et al.[19] measured the electron injection dynamics from PbS QDs anchored on amorphous titanium dioxide film using bifunctional linker molecule. Slow electron transfer of 100 ns was observed for PbS QDs with size below 4.3 nm. Plass et al.[20] studied synthesized PbS QDs in TiO_2 films without linker molecules. They attributed a time constant of 10 ps to electron injection from the QDs to the TiO_2 films based on transient absorption spectroscopy.

Based on molecular dynamics simulations, a sub-50 femtosecond time constant for electron injection from PbSe QDs into rutile (110) TiO_2 was reported.[21] Recently, Lian and co-workers[22] showed that the excitonic absorption of PbS QDs was pronouncedly broadened, which was due to strong mixing of the QD and TiO_2 conduction band levels. As a result, ultrafast electron transfer between QDs and TiO_2 was reported.

In this paper, we studied the charge separation in PbS QDs/TiO_2 heterojunction solar cell using ultrafast transient absorption measurements. Photoinduced interfacial electron injection at the surface of two different TiO_2 crystallographic planes was investigated; the more abundant (101) anatase crystallographic facets and the (001) crystallographic facets. Ultrafast laser pump-probe measurements revealed faster electron injection from PbS QDs to the (001) TiO_2 facet than to (101) TiO_2 facet, which supports the superior photocurrent generation in PbS QDs/(001) TiO_2 heterojunction solar cell. Photovoltaic measurements showed enhanced performance for the PbS QDs/(001) TiO_2 heterojunction solar cell than the PbS QDs/(101) TiO_2 heterojunction solar cell, mainly due to higher current density.

2. Results and Discussion

The characterization of TiO_2 nanosheets was reported in our previous publication.[12] As discussed earlier, the X-ray diffraction (XRD) pattern of TiO_2 nanosheets synthesized at 180 °C shows that the obtained product was pure anatase TiO_2 nanosheets. The lattice spacing was determined to be 0.235 nm, corresponding to the (001) planes of anatase TiO_2 and the corresponding selected-area electron diffraction (SAED) pattern further indicates that the top and bottom facets of the nanosheets are the (001) planes. The nanosheets consist of well-defined rectangular sheet-like structures with a side length of 30 nm and a thickness of 7 nm. The percentage of highly reactive (001) facets in the TiO_2 nanosheets was estimated to be 65% according to the above structural information. **Figure 1** shows the transmission electron microscopy (TEM) image of the TiO_2 nanosheets.

The prepared TiO_2 nanosheets were used for the fabrication of PbS QDs/TiO_2 heterojunction solar cells. **Figure 2**A presents a device structure and scheme of the energy level diagram. The bottom layer is composed of compact TiO_2 and TiO_2 nanosheets with exposed (001) facets acting as electron collectors, as a reference, devices with exposed (101) facets were studied. The

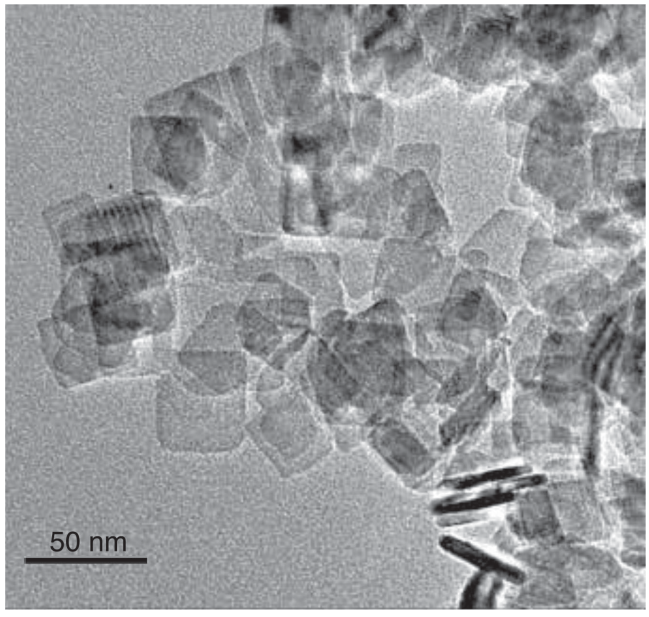

Figure 1. TEM image of 30 nm TiO_2 nanosheets used in this study.

light is absorbed by PbS QDs film, which was made using the layer-by-layer deposition technique. The original ligands of the PbS QDs (oleic acid) were replaced by MPA during deposition. A gold contact was evaporated on top of the PbS QDs film. After absorption of light, electrons are injected to the TiO_2 while holes are transported to the gold contact.

We have performed an in-depth study of the electron injection process from the PbS QDs to the TiO_2 nanosheets (exposed facets 001) and to the TiO_2 NPs (exposed facets 101). In these devices, no hole-conducting layer is used. Therefore, the charge separation happens only at the QD/TiO_2 interface, and the holes have to transfer through the QD film to the gold contact. In order to have electron injection from QDs into TiO_2 films, the energy of photo-excited electrons in the $1S_e$ QD level should exceed the energy of the TiO_2 conduction band edge. This condition is fulfilled in the case of PbS-TiO_2 system (Figure 2A). The driving force for electron injection process is governed by the difference between QD conduction band and TiO_2

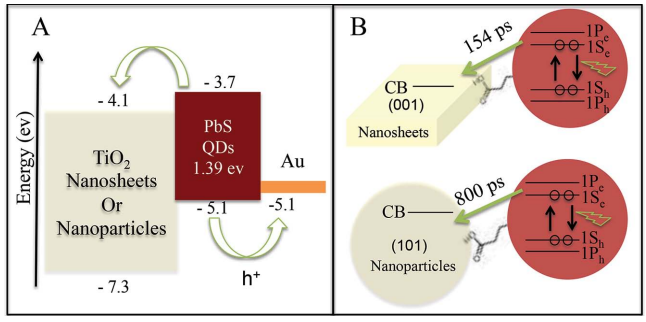

Figure 2. A) Schematic illustration of the energy level diagram of the PbS QDs/TiO_2 heterojunction solar cell. The positions of the energy levels were taken from ref. [12]. B) Illustration of the injection time from PbS QDs to 001 TiO_2 nanosheets and 101 TiO_2 nanoparticles. ps- picoseconds, CB-conduction band.

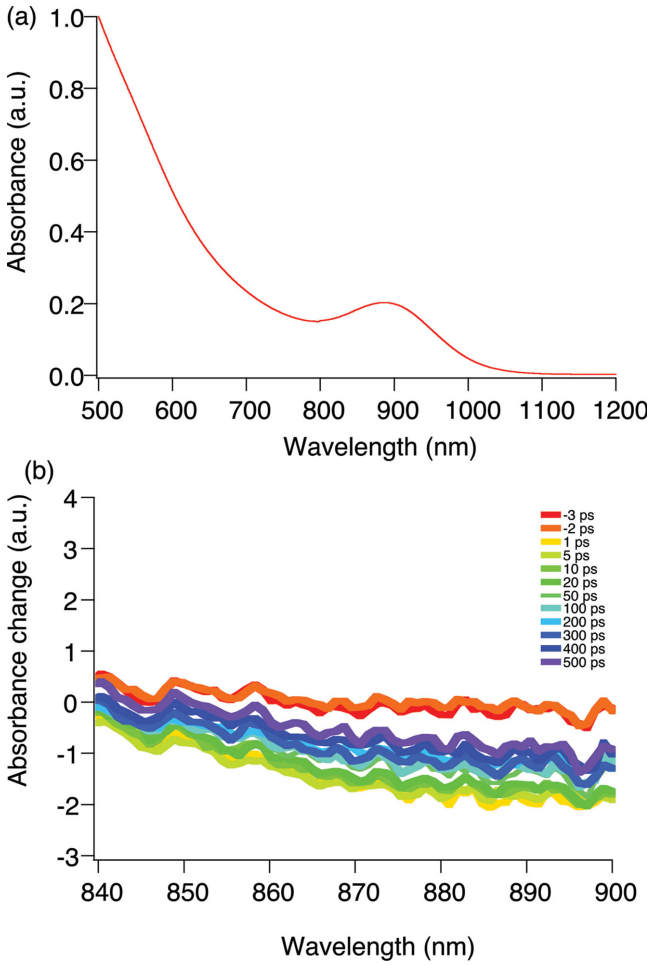

Figure 3. A) Absorption spectra of the PbS nanoparticles used in this study. B) Transient supercontinuum spectrum on PbS/TiO_2 heterojunction film. PbS QDs are excited at 520 nm, and the transient spectrum is shown at wavelengths from 840 to 900 nm centered the excitonic absorption peak. The negative traces show the absorption bleach formation and recovery in QDs due to laser-induced exciton formation and exciton dissociation via electron injection. Traces are recorded from excitation time up to 500 ps after excitation.

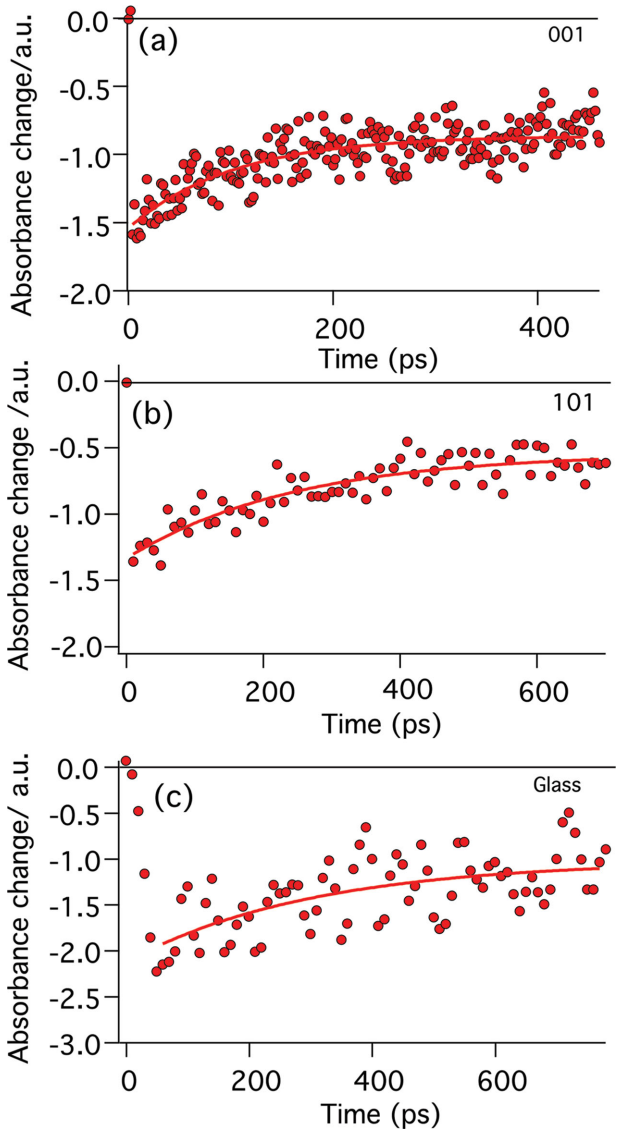

Figure 4. Bleaching dynamics for first excitonic transition ($1S_h$-$1S_e$) recorded at 870 nm following 520 nm excitation of PbS QD anchored on TiO_2 (001) nanosheets, (101) nanoparticles films and on top of a glass substrate. The absorbance bleach recovery is fitted by single exponential function. The solid lines represent the single exponential fitting. The fitting parameters are listed in Table 2.

conduction band. The conduction band position in QDs is size dependent and is very much affected by quantization. In this study, we used 3 nm PbS QDs (corresponding to band gap of 1.38 eV) linked to TiO_2 particles with different dominant crystallographic facets. **Figure 3**A showed typical absorption spectra of the studied PbS QDs; the first excitonic absorption peak is observed around 880 nm.

To determine the electron injection rate from PbS QDs into the (001) TiO_2 nanosheets and to the (101) TiO_2 NPs, time-resolved transient absorption measurements were performed. The PbS QDs were photo-excited with ultra short 520 nm laser pulses. Upon excitation, electron and hole accumulate in the conduction band and valence band, which induce a decrease of the absorption (bleaching) of QDs at wavelengths corresponding to the exciton absorption band. This absorption feature is in the wavelength range of 840 nm–1 μm. Transient absorption spectra in the NIR are displayed in Figure 3B. Monitoring the time evolution of the absorption bleaching gives information on charge-separation and recombination processes.

Figure 4 compares the transient absorption at 870 nm of the PbS QDs deposited on TiO_2 nanosheets with (001) dominant facets and TiO_2 NPs with (101) dominant facets. The PbS QDs and sample preparation are identical in both samples. These measurements were compared with that of PbS QDs deposited on glass prepared at identical experimental condition.

The transient absorption decay kinetic for each sample was fitted by single exponential decay function with exponential rate constant (τ^{-1}) and characteristic lifetime (τ) listed in **Table 1**.

For PbS QDs film on a glass substrate, the first-order rate constant (τ^{-1}) is 3.3×10^9 s^{-1} and increases to 4.1×10^9 s^{-1} and 9.8×10^9 s^{-1} when the QDs are anchored on the (101) and (001)

Table 1. Fitting parameters of the transient absorbance signals. τ^{-1} is the first-order rate constant of single exponential fit function to the transient absorptions signals. k_{et} is the interfacial electron-transfer deduced from Equation (1). τ_{et} is the characteristic time constant of interfacial electron-transfer process.

Sample	τ^{-1} [s^{-1}]	k_{et} [s^{-1}]	τ_{et} [s]
PbS/TiO_2 (001)	9.8×10^9	6.5×10^9	154×10^{-12}
PbS/TiO_2 (101)	4.1×10^9	0.8×10^9	800×10^{-12}
PbS/Glass	3.3×10^9	–	–

TiO_2 films, respectively. For PbS QDs deposited on glass, the recovery of the decay kinetics gives information on charge carrier processes in QDs, such as trapping of photoinduced carriers within the QDs,[18] followed by radiative recombination kinetic at longer time scale. When PbS QDs are in the vicinity of TiO_2 with lower lying conduction band, time-resolved signal is a convolution of both the interfacial electron-transfer rate and exciton recombination or charge trapping in QDs. Therefore, the acceleration in the observed rate constant is due to the additional charge-transfer pathway from QDs into the TiO_2. Therefore, the charge transfer rate constant can be estimated by Equation (1), with assuming that the entire carrier processes in QDs/glass sample and QDs/TiO_2 films are identical except the electron-transfer process.

$$k_{et} = \frac{1}{\tau(\mathrm{PbS} + \mathrm{TiO_2})} - \frac{1}{\tau(\mathrm{PbS})} \quad (1)$$

Using the rate constants values listed in Table 1, we obtained electron-transfer time constants of 800 ps and 154 ps for (101) and (001) TiO_2 films, respectively (see Figure 2B). These results indicate that there is a noticeable difference in electron injection time from PbS QDs to TiO_2 nanostructured films with different morphologies and crystallographic facets.

In order to learn the difference in the photovoltaic performance of these two TiO_2 crystalographic facets, solar cells using the studied PbS QDs were fabricated. The current–voltage characteristic of the cells made with (001) TiO_2 nanosheets and standard cells made of TiO_2 NPs with dominant exposed (101) facets (Dyesol paste DS90) are presented in **Figure 5**. The photovoltaic parameters of these cells are summarized in Table 1.

We observe that the TiO_2 nanosheets give higher short-circuit photocurrent than the standard TiO_2 NPs and better power conversion efficiency. These results are in agreement with previous studies that reported a better photovoltaic performance in (001) nanosheets than standard (101) nanoparticles, when the films are applied in both dye and QD-sensitized device configurations.[12,16] Our observation on the better interfacial charge separation at PbS/(001) nanosheets is consistent with the better photocurrent generation in these cells respect to the classical (101) nanoparticles-based devices. Studies by Kavan and co-workers[16] show that the electron transport is the same in these two film morphologies. Therefore, the faster charge separation kinetic for the nanosheets with (001) dominant facets supports the higher photocurrent achieved in the case of PbS QDs/TiO_2 nanosheets heterojunction solar cells compare to PbS QDs / TiO_2 NPs heterojunction solar cells.

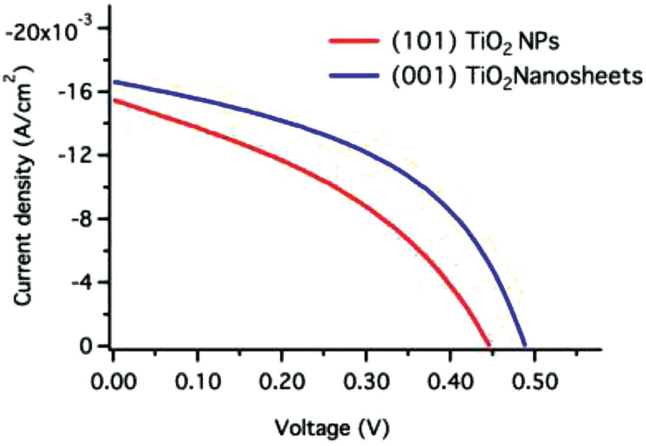

Figure 5. J–V curves of cells made of (001) TiO_2 nanosheets and standard cells made of TiO_2 NPs with dominantly exposed (101) facets.

It should be noted that the PbS QDs are attached to TiO_2 nanoparticles through a bifunctional linker molecule (MPA) that has a thiol group (SH) on one end and carboxylic group on the other side for anchoring to TiO_2. This molecule may contribute to additional deactivation pathway and also decrease the injection rate by increasing the donor–acceptor distance for electron transfer. Moreover, the thiol head groups can act as a hole scavenger if the oxidation potential is appropriate for hole-transfer reaction. The oxidation potential of thiol ligands is located between –5.5 and –6.0 eV versus vacuum.[19] The HOMO level of the PbS QDs used in this study located at –5.1eV (see Figure 2B); consequently the hole-transfer reaction is not favorable to occur in this system.

To rationalize the observed faster charge injection in DSCs based on nanosheets respect to nanoparticles, the QD anchoring geometry should be considered. For the electron injection into a continuum of acceptor states implies that the nuclear factor in Fermi golden rule is very large. For a through space tunneling, the electron-transfer rate is controlled by the electronic coupling between the donor and the acceptor states through ($\exp^{-\beta r}$), where r is the distance and β is the damping factor ($\beta \approx 1.2$ A^{-1}). The observed increase of the electron-transfer rate constant by a factor of 5, corresponds then to a decrease of the electron-transfer distance of about 1.4 Å, which can originate from different association geometry of MPA-capped PbS QDs on two different TiO_2 films. It can be hypothesized that the more closely exposed Ti_{5c} sites at (001) crystalline surface provide a better anchoring of the QDs to the (001) films via MPA linker molecule. A more precise theoretical modeling of the association geometry of QDs to the TiO_2 (001) and (101) surface via MPA linker molecule would be the subject of a separate study. In our previous publication on DSCs-based nanosheets, it was observed that the back electron transfer was by a factor of 6 slower for the TiO_2 (001) nanosheets compared to the same process on TiO_2 (101) NPs, that was rationalized by different association of carboxylic anchoring group on the two films of TiO_2. The different anchoring geometry of carboxylic on the two crystalline films was also proved by theoretical investigations using DFT techniques by De Angelis and co-workers.[24]

Table 2. Photovoltaic parameters for the (001) TiO_2 nanosheets cells and standard cells made of TiO_2 NPs with dominantly exposed (101) facets.

TiO_2 Sample	QDs E_g [eV]	V_{oc} [V]	Jsc [mA cm^{-2}]	FF	η [%]	BET [$m^2 g^{-1}$]
TiO_2 18 nm NPs (DS90)	1.38	0.44	15.48	0.38	3.32	75
TiO_2 nanosheets (001) dominant facets	1.38	0.49	16.63	0.46	4.17	122

In addition to photocurrent enhancement, the open circuit voltage was increased by 50 mV for the PbS/(001) TiO_2 solar cell compare to the PbS/(101) TiO_2 solar cell (see **Table 2**). This is again consistent with our previous work[16] on Ru-based DSCs where higher *Voc* was also achieved for Ru-sensitized (001) TiO_2 nanosheet photoanode respect to Ru-sensitized (101) TiO_2 NPs. The higher *Voc* was rationalized by a negative shift in the conduction band of the TiO_2 nanosheets with (001) dominant facets compared to the TiO_2 NPs with (101) dominant facets, which was later proved by the theoretical analysis based on density functional theory calculations by De Angelis and co-workers.[24]

Finally, the PbS/(001) TiO_2 heterojunction solar cell demonstrates better quantum yield (Φ_{inj}) for charge injection. The quantum yield for charge injection into TiO_2 depends upon the kinetic competition between interfacial electron- transfer rate (k_{et}) and recombination rate (k_r) within the QDs given by Equation (2). The recombination rate constant, $k_r \approx \tau^{-1}$, was measured for the PbS QDs on glass substrate. Therefore, the quantum yield of charge injection was calculated to be 0.75 for (001) nanosheets and 0.55 for (101) NPs, which agree well with the better PV performance of the PbS/(001) TiO_2 heterojunction solar cells.

$$\Phi_{inj} = \frac{k_r}{k_r + k_{et}} \tag{2}$$

To summarize, this report provides complementary understanding to the existing studies on charge separation in QDs based solar cells, it uses pump probe laser spectroscopy to elucidate the interfacial charge separation at different TiO_2 crystallographic facets in heterojunction PbS QDs solar cell.

3. Conclusion

This work describes for the first time the rate of electron transfer from PbS QDs to different TiO_2 crystallographic facets in PbS QDs heterojunction solar cell. Two different TiO_2 dominant facets were studied, the TiO_2 (101) exposed facets and the TiO_2 (001) exposed facets. The electron-transfer rate from the PbS QDs to the (001) exposed facets was faster by a factor of 5 than the electron-transfer rate to the (101) exposed facets. This observation is consistent with the higher current density and the better power conversion efficiency observed in the PbS QDs/(001) TiO_2 heterojunction solar cells. Moreover, the quantum yield for charge injection was higher for the (001) dominant facets compare to the (101) dominant facets, which further support the better PV performance. This work demonstrates that the TiO_2 nanosheets with exposed (001) facets can be a better alternative to the conventional (101) TiO_2 NPs in QDs and possibly in perovskite-based solar cells.

4. Experimental Section

Synthesis and Purification of TiO_2 Nanosheets: The synthesis of TiO_2 nanosheets followed a typical experimental procedure.[15] 10 mL of Ti(OBu)4 (98%) and 0.8 mL of hydrofluoric acid (47%) solution were mixed in 150 mL dried Teflon autoclave, which was kept at 180 °C for 24 h to yield the nanosheets. After the reaction mixture was cooled to room temperature, the white powder was separated by high-speed centrifugation and washed with ethanol followed by distilled water for several times.

Caution: Hydrofluoric acid is extremely corrosive and a contact poison, it should be handled with extreme care! Hydrofluoric acid solution is stored in Teflon containers in use.

Methods and Device Fabrication: Colloidal PbS QDs were purchased from Evident Technology and were kept under inert atmosphere. During device fabrication, a thin blocking layer of compact TiO_2 was first deposited by spray pyrolysis onto a precleaned FTO glass substrate using a solution of titanium diisopropoxide bis(acetylacetonate) in ethanol as precursor. Finally, a layer of TiO_2 nanosheets was deposited by spin-coating (4000 rpm for 10 s) from dilute aqueous solution containing a mixture of TiO_2 nanosheets and ethanol (volume ratio of 1:3). This results in a nanosheet titania film with 300 ± 50 nm thickness. The procedure for the deposition of the PbS QDs film is adapted from the one reported by Sargent and co-workers.[23] The PbS QDs were subsequently deposited layer by layer on the porous TiO_2 film by spin coating a 50 mg mL^{-1} solution in octane. Each layer was casted at a spinning rate of 2500 rpm applied for 10 s and treated thereafter briefly with a solution of 10% 3-mercaptopropionic acid (MPA, ≥99.0% from Sigma–Aldrich) in methanol using again 2500 rpm rotational speed for 10 s. This treatment displaced the oleate ligand and rendered the QD insoluble, which allowed thin films of 300 nm thicknesses to be created using 12 successive deposition cycles. Each layer was rinsed with anhydrous methanol (purchased from Sigma–Aldrich) to remove excess of MPA and PbS QDs. Finally, gold back contact of ≈100 nm thicknesses was deposited by evaporation through a shadow mask. The device was then completed by encapsulation in an argon atmosphere. The device was encapsulated by gluing a 2-mm thick glass plate on top of the active area of the device using a frame of hot melt Surlyn (25 μm thick) as a sealant and spacer. After encapsulation, the device was stable in ambient air.

Photovoltaic Characterization: Photovoltaic measurements employed an AM 1.5 solar simulator equipped with a 450 W xenon lamp (Model No. 81172, Oriel). Its power output was adjusted to match AM 1.5 global sunlight (100 mW cm^{-2}) by using a reference Si photodiode equipped with an IR-cutoff filter (KG-3, Schott) in order to reduce the mismatch between the simulated light and AM 1.5 (in the region of 350–750 nm) to less than 2% with measurements verified at two PV calibration laboratories [ISE (Germany), NREL (USA)]. I–V curves were obtained by applying an external bias to the cell and measuring the generated photocurrent with a Keithley model 2400 digital source meter. The voltage step and delay time of photocurrent were 10 mV and 40 ms, respectively. Photovoltaic performance was measured by using a metal mask with an aperture area of 0.12 cm^2.

Pump-Probe Laser Spectroscopy: Time-resolved transient absorption measurements were performed on PbS QDs (0.5 μm thick)/TiO_2

mesoporous heterojunction films. The pump-probe spectroscopy technique used a CPA-2001, 1 kHz repetition rate, Ti: Sapphire amplified femtosecond laser (Clark-MXR), delivering 1 mJ pulses of 150 fs width at a central wavelength of 775 nm. The excitation beam was provided by pumping a double-stage noncollinear optical parametric amplifier (NOPA). The NOPA was tuned at 530 nm to generate pulses of approximately 8 μJ energy, which were then compressed in an SF10-glass prism pair down to a duration of less than 60 fs (fwhm). As the probe beam, a white light continuum was generated by focusing a small fraction of 775 nm pulses from the CPA laser system by a f = 50 mm lens into a 2-mm-thick CaF_2 rotating disc. The time delay between excitation and probe pulses was controlled precisely be means of a motorized translation stage (M531 PD, Physik Instrument) equipped with a retro-reflector (49-668, Edmund Optics). At the sample, pulse energy was decreased down to a few microjoules for the pump and to less than 1 μJ for the probe beam. Transient absorption spectra were calculated from shot-by-shot simultaneous measurements of signal and reference beams using a pair of spectrographs (Princeton Instruments, SpectraPro 2150) equipped with 512 × 58 pixels back-thinned CCD detectors (Hamamatsu S7030-0906) and by chopping the probe beam at a frequency of 500 Hz. Time-resolved experiments were applied on sealed samples.

Acknowledgements

The authors acknowledge Dr. M. K. Nazeeruddin for fruitful discussions. L.E. thanks the Marie Curie Actions—Intra-European Fellowships (FP7-PEOPLE-2009-IEF) under grant agreement no. 252228, project "Excitonic Solar Cell." M.G. thanks the European Research Council for financial support under the Advanced Research Grant "Mesolight." L.E acknowledges the Israel Alternative Energy Foundation (I-SAEF) that financed this research and to the Office of the Chief Scientist of the Ministry of Industry, Trade, and Labor Kamin project no. 50303, and the Tashtiot project by the Chief Scientist of the Ministry of Industry. B.L. thanks Singapore-Berkley Energy Research Programme (R279-000-393-592) for financial support.

Received: September 23, 2014
Published online: November 11, 2014

[1] F. W. Wise, *Acc. Chem. Res.* **2000**, *33*, 773.
[2] M. A. Hines, G. D. Scholes, *Adv. Mater.* **2003**, *15*, 1844.
[3] J. M. Pietryga, R. D. Schaller, D. Werder, M. H. Stewart, V. I. Klimov, J. A. Hollingsworth, *J. Am. Chem. Soc.* **2004**, *126*, 11752.
[4] R. Schaller, V. Klimov, *Phys. Rev. Lett.* **2004**, *92*, 186601.
[5] A. Kongkanand, K. Tvrdy, K. Takechi, M. Kuno, P. V. Kamat, *J. Am. Chem. Soc.* **2008**, *130*, 4007.
[6] A. J. Nozik, *Annu. Rev. Phys, Chem.* **2001**, *52*, 193.
[7] Y. Liu, M. Gibbs, J. Puthussery, S. Gaik, R. Ihly, H. W. Hillhouse, M. Law, *Nano Lett.* **2010**, *10*, 1960.
[8] I. J. Kramer, L. Levina, R. Debnath, D. Zhitomirsky, E. H. Sargent, *Nano Lett.* **2011**, *11*, 3701.
[9] H. Liu, J. Tang, I. J. Kramer, R. Debnath, G. I. Koleilat, X. Wang, A. Fisher, R. Li, L. Brzozowski, L. Levina, E. H. Sargent, *Adv. Mater.* **2011**, *23*, 3832.
[10] J. Gao, J. M. Luther, O. E. Semonin, R. J. Ellingson, A. J. Nozik, M. C. Beard, *Nano Lett.* **2011**, *11*, 1002.
[11] J. Gao, C. L. Perkins, J. M. Luther, M. C. Hanna, H.-Y. Chen, O. E. Semonin, A. J. Nozik, R. J. Ellingson, M. C. Beard, *Nano Lett.* **2011**, *11*, 3263.
[12] L. Etgar, W. Zhang, S. Gabriel, S. G. Hickey, M. K. Nazeeruddin, A. Eychmüller, B. Liu, M. Grätzel, *Adv. Mater.* **2012**, *24*, 2202.
[13] E. Ghadiri, N. Taghavinia, H. R. Aghabozorg, A. Iraji zad, *Eur. Phys. J. Appl. Phys.* **2010**, *50*, 20601.
[14] E. Ghadiri, N. Taghavinia, S. M. Zakeeruddin, M. Grätzel, J.-E. Moser, *Nano Lett.* **2010**, *10*, 1632.
[15] L. Etgar, P. Gao, Z. Xue, Q. Peng, A. K. Chandiran, B. Liu, M. K. Nazeeruddin, M. Grätzel, *J. Am. Chem. Soc.* **2012**, *134*, 17396.
[16] B. Laskova, M. Zukalova, L. Kavan, A. Chou, P. Liska, Z. Wei, L. Bin, P. Kubat, E. Ghadiri, J.-E. Moser, *J. Solid State Electrochem.* **2012**, *16*, 2993.
[17] I. Robel, M. Kuno, P. V. Kamat, *J. Am. Chem. Soc.* **2007**, *129*, 4136.
[18] K. Tvrdy, P. A. Frantsuzov, P. V. Kamat, *Proc. Natl. Acad. Sci. USA* **2011**, *108*, 29.
[19] B. R. Hyun, Y. W. Zhong, A. C. Bartnik, L. Sun, H. D. Abruña, F. W. Wise, J. D. Goodreau, J. R. Matthews, T. M. Leslie, N. F. Borrelli, *ACS Nano* **2008**, *2*, 2206.
[20] R. Plass, S. Pelet, J. Krueger, M. Grätzel, *J. Phys. Chem. B* **2002**, *106*. 7578.
[21] R. Long, O. V. Prezhdo, *J. Am. Chem. Soc.* **2011**, *133*, 19240.
[22] Y. Yang, W. Rodriguez- Cordoba, X. Xiang, T. Lian, *Nano Lett.* **2012**, *12*, 303.
[23] A. G. Pattantyus-Abraham, I. J. Kramer, A. R. Barkhouse, X. Wang, G. Konstantatos, R. Debnath, L. Levina, I. Raabe, M. K. Nazeeruddin, M. Grätzel, E. H. Sargent, *ACS Nano* **2010**, *4*, 3374.
[24] F. De Angelis, G. Vitillaro, L. Kavan, M. K. Nazeeruddin, M. Grätzel, *J. Phys. Chem. C* **2012**, *116*, 18124.